Chemical Engineering Journal 431 (2022) 134207

Contents lists available at ScienceDirect

Chemical Engineering Journal

journal homepage: www.elsevier.com/locate/cej

# Dual sulfur-doped sites boost potassium storage in carbon nanosheets derived from low-cost sulfonate

Zijian Li [a,1], Xinfei Wu [b,1], Wen Luo [a,c,*], Chenxu Wang [c], Wencong Feng [a], Xufeng Hong [d], Liqiang Mai [a,*]

[a] State Key Laboratory of Advanced Technology for Materials Synthesis and Processing, School of Materials Science and Engineering, Wuhan University of Technology, Wuhan 430070, PR China
[b] State Key Laboratory of Advanced Technology for Materials Synthesis and Processing, International School of Materials Science and Engineering, Wuhan University of Technology, Wuhan 430070, PR China
[c] Department of Physics, School of Science, Wuhan University of Technology, Wuhan 430070, PR China
[d] School of Materials Science and Engineering, Peking University, Beijing 100871, PR China

ARTICLE INFO

*Keywords:*
Potassium-ion battery
Carbon nanosheets
Anode
Dual sulfur-doping
One-step pyrolysis

ABSTRACT

As a new energy storage system, K-ion batteries (KIBs) have the advantages of low price and competitive high energy density. However, due to the large radius of $K^+$, in the process of intercalation/deintercalation, the traditional carbon anode materials usually display insufficient cycle life and poor rate performance in KIBs. In this work, inexpensive and widely-sourced sodium p-toluenesulfonate ($CH_3C_6H_4SO_3Na$) is used as raw material to synthesize dual sulfur-doped carbon nanosheets (DS-CN) by a simple one-step carbonization method. The nanosheets possess an enlarged interlayer distance (4.25 Å) which allows large $K^+$ to intercalate. C-S bonds and the embedded ultrafine sulfate provide active sites to enhance capacity and accelerate kinetics. Moreover, a high S/O ratio would reduce the irreversible reactions caused by oxygen functional groups. The high reversible specific capacity (331.9 mA h $g^{-1}$ at 50 mA $g^{-1}$), good rate performance (165.3 mA h $g^{-1}$ at 1000 mA $g^{-1}$) and long cycle stability (0.011% capacity decay per cycle) are attributed to the multiple synergistic effects of enlarged layer spacing, reaction between C-S bonds and $K^+$, as well as more active -C-$SO_2$- bonds, as confirmed by *ex-situ* XPS and electrochemical analysis. Our work shows a feasible and effective way to develop low-cost, high-performance carbon anode materials for KIBs.

## 1. Introduction

With the advent of energy era, the demand for sustainable and reliable energy storage and conversion devices is ever-increasing. Rechargeable Li-ion batteries (LIBs) play a pivotal part in the energy supply of portable electronic devices and large power grid [1,2]. However, the increasing shortage of lithium resources and uneven distribution lead to the surge in LIBs costs and challenge large-scale exploitation of lithium [3]. Therefore, it is urgent to develop a new-type battery system with crustal resources and sustainability. Currently, K-ion batteries (KIBs) stimulate interest in research due to its unique superiorities [4–7]. Since potassium and lithium locate in the group IA, they share homologous physiochemical properties and battery-operation principles. The advantages of KIBs include: (1) the abundance (1.5% of the Earth's crust element reserves, vs Li ~ 0.0065%) and evenly distribution of potassium ensure an adequate supply of raw materials. At present, the selling price of metal potassium is just one tenth of that of lithium metal. (2) The lower $K^+$/K redox potential than that of $Li^+$/Li in some non-aqueous electrolyte solvents enable a higher working voltage and greater specific energy for KIBs. For example, in ethylene carbon (EC)/diethyl carbonate (DEC), the $K^+$/K potential is 0.15 V lower than $Li^+$/Li [8,9]. (3) Although the radius of $K^+$ (1.38 Å) is not as small as that of $Li^+$ (0.76 Å) , while the solvated ion formed by $K^+$ in electrolyte solvent is much smaller due to its weaker Lewis acid nature, which contributes to higher ionic conductivity [10]. Therefore, faster diffusion kinetics and high-rate performance are expected to obtain due to

* Corresponding Authors at: State Key Laboratory of Advanced Technology for Materials Synthesis and Processing, School of Materials Science and Engineering, Wuhan University of Technology, Wuhan 430070, PR China.
*E-mail addresses:* luowen_1991@whut.edu.cn (W. Luo), mlq518@whut.edu.cn (L. Mai).
[1] Zijian Li and Xinfei Wu contributed equally to this work.

https://doi.org/10.1016/j.cej.2021.134207
Received 21 October 2021; Received in revised form 8 December 2021; Accepted 13 December 2021
Available online 16 December 2021

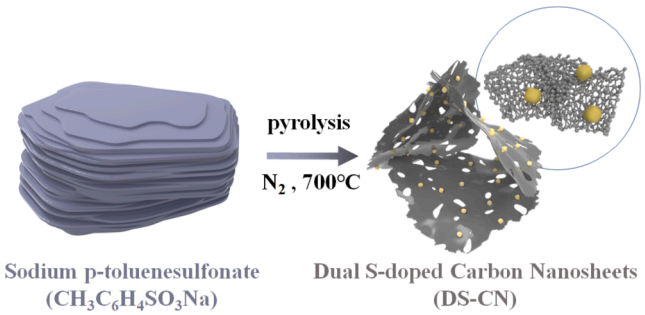


**Fig. 1.** Schematic illustration of the synthesis of DS-CN.

enhanced ionic conductivity. However, for graphite successfully commercialized as anode in LIBs, the repeated intercalation/deintercalation of large ion radius of $K^+$ will cause huge volume changes and result in material structure damage, poor cycle stability and short service life of KIBs [8]. Therefore, to develop anode materials with low cost, stable structure and excellent performance is crucial in KIBs technology.

At present, researchers have widely studied the anode electrode materials of KIBs, such as carbon [11], metal compounds [12], alloys [13], organic compounds [14] and so on. Among them, carbon-based materials (including graphite [15], graphene [16], carbon-microspheres [17], carbon-fibers [18], carbon-nanotubes [19] and other carbon-based composites [20]) have been focused owing to their advantages of low cost, high conductivity and outstanding cycle stability. Particularly, carbon materials with heteroatoms doped have been intensively studied in order to further adjust chemical environment and improve electrochemical performance. Common non-metallic heteroatoms such as boron [21], nitrogen [22–24], phosphorus [25–27], sulfur [28] and oxygen [29] can improve wettability and conductivity of carbon materials to a certain extent, and are expected to provide more defects and potassium storage sites, so as to improve the reversible capacity. For example, Liu *et al.* synthesized N-doped soft carbon as anode electrode whose reversible capacities was 266 mA h $g^{-1}$ at 100 mA $g^{-1}$ in KIBs [22]. Yan *et al.* synthesized S-doped graded porous carbon with high defect density area as the anode electrode of KIBs, which exhibited a capacity of 197.0 mA h $g^{-1}$ under 100 mA $g^{-1}$ [30]. More importantly, dual-doping strategy has demonstrated great capability in tailoring local electronic structure (physically) and introducing surface functional groups (chemically) [31–34]. For example, Yang *et al.* prepared $NH_2$-MIL-101(Al) precursor by solvothermal method, and then obtained a N/O dual-doped carbon through carbonization. N/O dual-doped carbon provided 230 mA h $g^{-1}$ after 100 cycles at 50 mA $g^{-1}$ [29].

However, with regards to prepare dual-doping pyrolytic carbon precursors, the expensive raw materials, complex processes and long-time reactions are usually involved, such as mental-organic frameworks (MOFs) precursor. To find a cheap and easily available raw material and adopt a feasible preparation process are the key to the research of carbon anode for KIBs. Moreover, as discussed above, sulfur doping holds great promise in tailoring carbonaceous anodes, while the novel dual-sulfur doping carbon with versatile configurations still remains to be investigated.

Herein we demonstrate a one-step low-cost pyrolysis to obtain dual S-doped carbon nanosheets (DS-CN) as anode for high performance KIBs. And we investigate kinetics and electrochemical reaction mechanism via *ex-situ* characterizations and electrochemical analysis to expound the effect of dual S-doping, which can offer a new approach to develop and update KIBs technology.

## 2. Results and discussion

Fig. 1 shows the synthesis process of DS-CN. Sodium p-toluenesulfonate ($CH_3C_6H_4SO_3Na$) is calcined by a simple one-step method, and the final product is obtained after washing with hydrochloric acid, water and isopropanol (the preparation of S-CB (the pyrolysis product of p-toluenesulfonic acid ($CH_3C_6H_4SO_3H$)) is same as DS-CN). Fig. 2**a** exhibits the X-ray diffraction (XRD) patterns of pyrolytic carbons synthesized from two raw materials. Two broad diffraction peaks ($2\theta \approx 22°$ and 43°) can be observed in both samples, which correspond to (0 0 2) and (1 0 0) crystal plane of graphite, respectively [35,36]. Compared with S-CB, the (0 0 2) diffraction peak of DS-CN shifts to the lower diffraction degree, which represents the increase of *d*-spacing. Referring to the calculation of Scherrer formula, the *d*-spacing ($d_{002}$) of DS-CN is 4.25 Å, which is much larger than that of S-CB (3.87 Å). According to the previous reports, the expanded interlayer spacing is beneficial to buffer the volume effect of $K^+$ in the charge/discharge process [37]. And the diffraction peak of DS-CN at $2\theta \approx 43°$ is not sharp, which proves that it possesses a disorder structure. This conclusion is proved by Raman

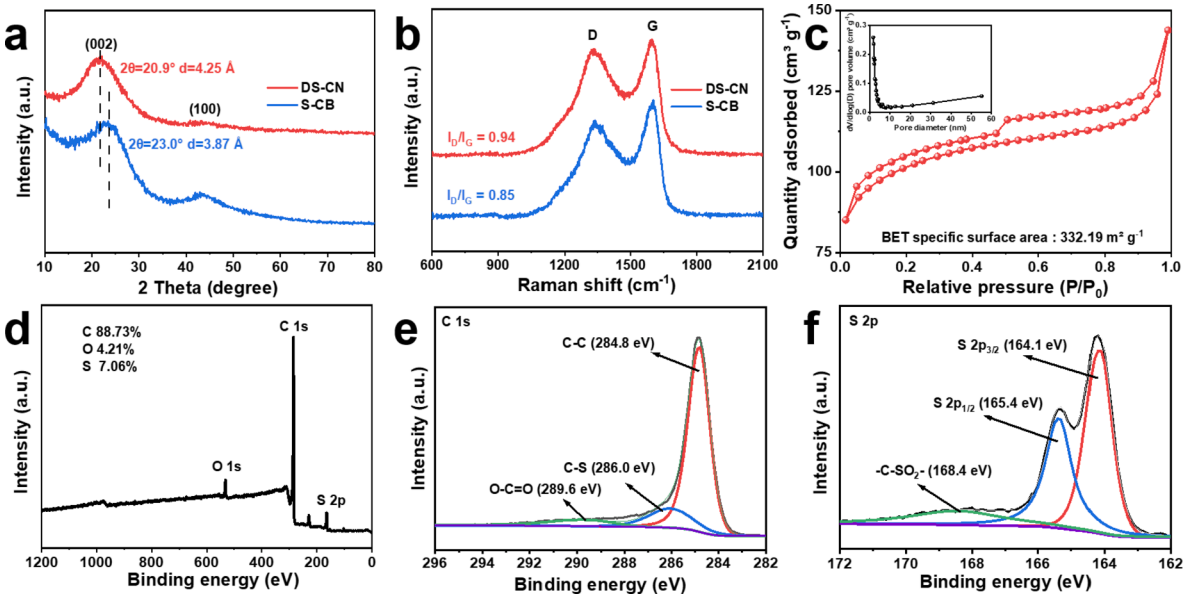


**Fig. 2.** Structure characterization: (a) XRD patterns of DS-CN (red) and S-CB (blue); (b) Raman spectra of DS-CN (red) and S-CB (blue); (c) $N_2$ adsorption/desorption isotherm and the corresponding pore size distribution of DS-CN; (d) Full-spectrum XPS survey, (e) C 1s, (f) S 2p of DS-CN. (For interpretation of the references to colour in this figure legend, the reader is referred to the web version of this article.)

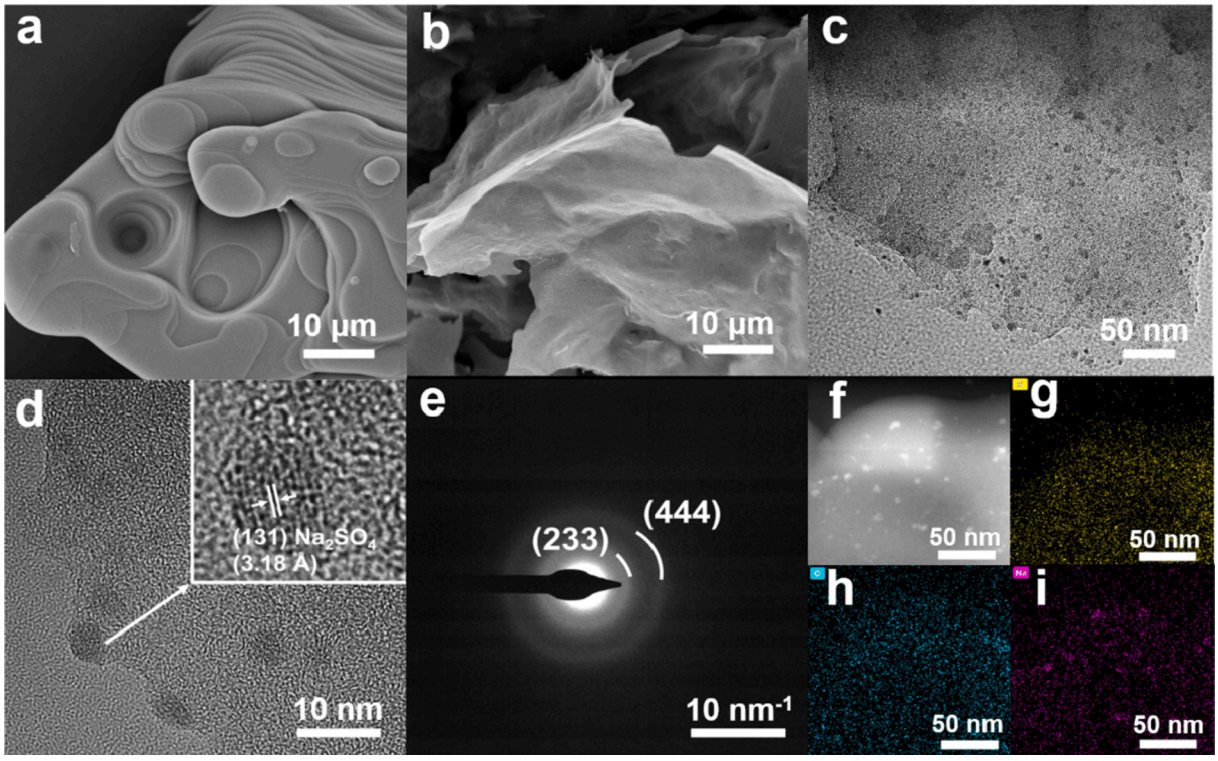


**Fig. 3.** Morphological characterization: SEM images of (a) $CH_3C_6H_4SO_3Na$ and (b) DS-CN; (c-d) HRTEM images of DS-CN; (e) SAED pattern of DS-CN; (f-i) Corresponding elemental mapping of S, O, and Na elements in DS-CN from the HRTEM image.

spectra in Fig. 2**b**. Both DS-CN and S-CB have typical D (≈ 1344 $cm^{-1}$) and G bands (≈ 1600 $cm^{-1}$) of carbon-based materials, where the former is correlated to the breathing vibration of k-point phonons, and the latter is associated with the conjugated mode of $sp^2$ carbon [38,39]. Therefore, the intensity ratio of D to G bands could reflect the structure defect and graphitization level of carbon-based materials. The $I_D/I_G$ ratio of DS-CN (0.94) is higher than that of S-CB (0.85), which means the vibration of disordered carbon is stronger.

To deeply analyze the structure of DS-CN, the $N_2$ adsorption–desorption isotherms (Fig. 2**c**) were characterized. The hysteresis loop exhibits that the sample possesses the characteristic of type IV isotherm [29]. The Brunauer-Emmett-Teller (BET) specific surface area of DS-CN is 332.19 $m^2\ g^{-1}$. The generated micropores are caused by the release of gas during hydrochloric acid washing. The gas was caused by the disproportionation of the intermediate products $Na_2S_2O_6$, and acidic solution can promote the reaction [40–42]. The high specific surface area and the pore structure are conducive to the sufficient contact with electrolyte and shorten ion transport distance [43]. To better characterize the structures, the FT-IR spectra (Fig. S1) of DS-CN and $CH_3C_6H_4SO_3Na$ were obtain. Compare with $CH_3C_6H_4SO_3Na$, a weak peak at 1385 $cm^{-1}$ was detected for DS-CN. And it is ascribed to C–S bond [32].

In order to further understand the chemical state of elements in the calcined materials, X-ray photoelectron spectroscopy (XPS) was measured to analyze the chemical composition. As shown in Fig. 2**d** and Fig. S2a, the relative atom ratios of S in DS-CN and S-CB are 7.06 at% and 2.41 at%, respectively. Furthermore, the atom ratios of O account for 4.21 at% and 15.62 at%, respectively. The results show that the S/O ratio in DS-CN is higher than that of S-CB. It has been studied that oxygen-containing functional groups would react with alkali-ion resulting in capacity loss, so DS-CN is expected to provide more reversible capacity [38,39]. The C 1s spectra (Fig. 2**e**) of DS-CN could be deconvoluted into three obvious peaks at 284.8 eV, 286.0 eV and 289.6 eV, corresponding to C–C, C-S and O-C=O bond respectively [44]. Fig. 2**f** shows that the S 2p spectrum of DS-CN is deconvoluted into three peaks and the peaks at 164.1 eV and 165.4 eV can be attributed to S $2p_{3/2}$ and S $2p_{1/2}$ of C-S-C bond, which are also ascribed as thiophene type sulfur. The other peak at 168.4 eV corresponds to -C-$SO_2$- bond, which is ascribed as oxidized-type sulfur [35]. The C-S bond has been proved to provide active sites for $K^+$ adsorption, while the -C-$SO_2$- bond with a stronger adsorption capability would react with $K^+$ to further enhance kinetic and capacity [38]. The O 1s spectra (Fig. S3) of DS-CN and S-CB could be deconvoluted into four obvious peaks, corresponding to O-S, C=O, C-OH and COOH bond respectively [44–46].

Fig. 3**a, b** and Fig. S4 present the scanning electron microscopy (SEM) images of $CH_3C_6H_4SO_3Na$ and DS-CN. The $CH_3C_6H_4SO_3Na$ powder is a massive structure formed by stacking sheets before carbonization. The sheets were peeled off during carbonization. The achieved DS-CN exhibits a thin nanosheet structure with the size of about 20 ~ 200 μm. Atomic force microscopy (AFM) image (Fig. S5) shows that the thickness of DS-CN is about 3.87 nm. The SEM and transmission electron microscopy (TEM) images of $CH_3C_6H_4SO_3H$ and its corresponding pyrolytic sample S-CB are shown in Fig. S6. $CH_3C_6H_4SO_3H$ powder is an irregular structure while S-CB is a polyhedral block structure. As shown in Fig. 3**c and d**, high resolution transmission electron microscopy (HRTEM) images of DS-CN show that uniformly dispersed nanoparticles with a diameter of about 3 ~ 5 nm are decorated on nanosheet. In order to analyze the crystalline state of DS-CN and the phase characteristics of the nanoparticles, HRTEM and selected region electron diffraction patterns (SAED) were recorded. As shown in Fig. 3**d**, DS-CN has no obvious lattice fringes, which proves that it has an amorphous structure. On the contrary, conspicuous lattice fringes can be observed at the nanoparticles. In Fig. S7, it is measured that the crystal plane spacing is 3.18 Å, which can correspond to the (1 3 1) crystal plane of orthorhombic $Na_2SO_4$ (JCPDS: 00–002-0839). In order to further verify the nanoparticle phase, two obvious diffraction rings in the SAED diagram in Fig. 3**e** correspond to the (2 3 3) and (4 4 4) planes of $Na_2SO_4$, respectively. The energy dispersive spectrometer (EDS) image of DS-CN shows that the S element (Fig. 3**g**) is evenly distributed in the sample. The strong signal of Na element in Fig. 3**i**

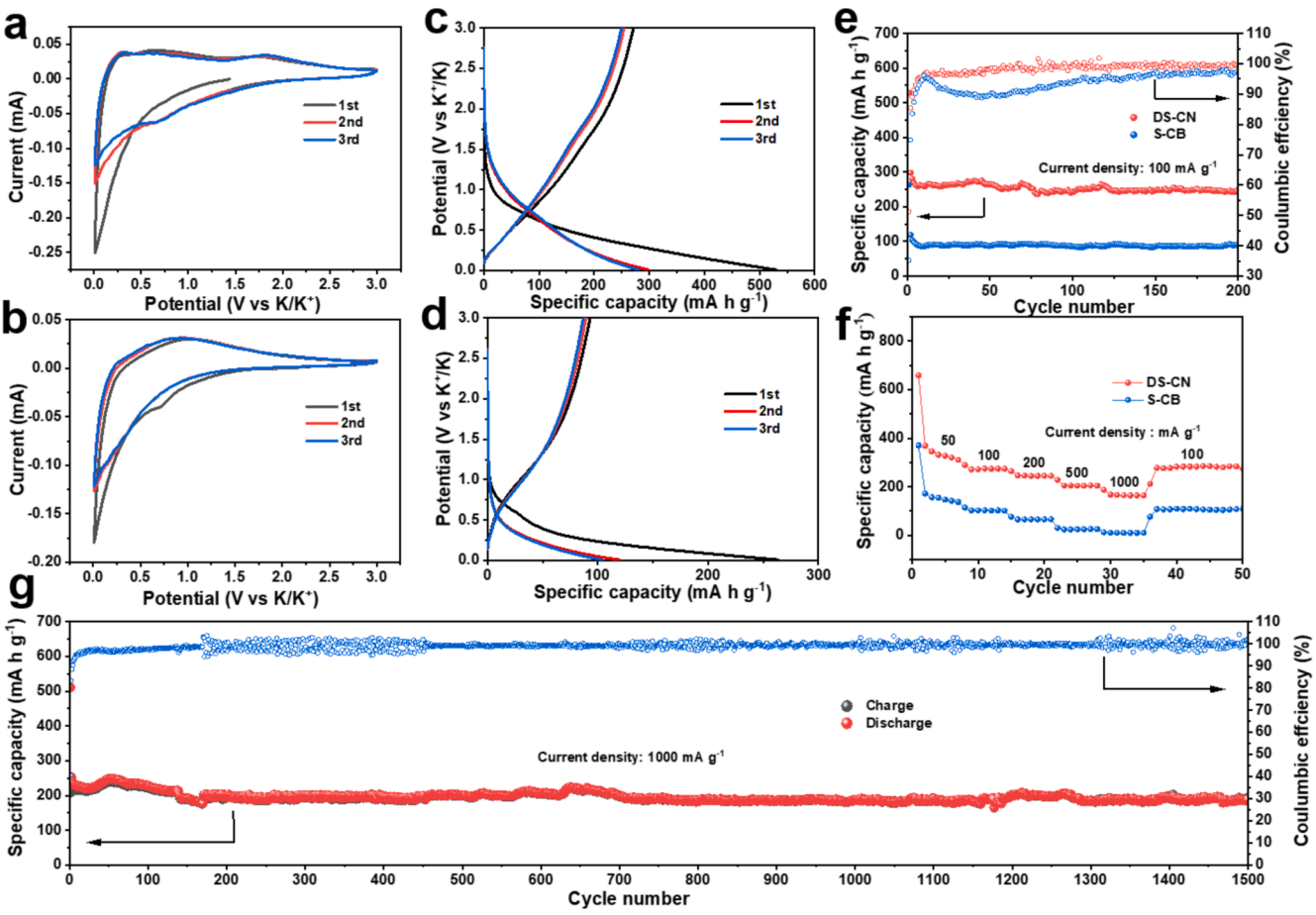


**Fig. 4.** The electrochemical performances in KIBs: The CV curves of (a) DS-CN and (b) S-CB at 0.1 mV $s^{-1}$; Charge–discharge curves of (c) DS-CN and (d) S-CB for the first three cycles at 100 mA $g^{-1}$; (e) Cycling performances of DS-CN (red) and S-CB (blue) at a current density of 100 mA $g^{-1}$; (f) Rate performances of DS-CN (red) and S-CN (blue) at various current densities; (g) Long-term cycling performance of DS-CN at a current density of 1000 mA $g^{-1}$. (For interpretation of the references to colour in this figure legend, the reader is referred to the web version of this article.)

further confirm that the ultrafine nanoparticles are $Na_2SO_4$. There are C-S and -C-$SO_2$- bond in material, which can prove that the $Na_2SO_4$ is not free, but strongly bond to carbon. The water contact angle test of DS-CN (Fig. S8) shows that it is a hydrophobic material. Therefore, the evenly distributed ultrafine sulfates can stably exist after acid washing. We believe that the mechanisms for the pyrolysis of the $CH_3C_6H_4SO_3Na$ is based on radical breakdown and recombination via the reaction [47]:

$$Ar\text{-}SO_3Na \rightarrow Ar\cdot + \cdot SO_3Na \quad (2.1)$$

$$\cdot SO_3Na + Ar\text{-}SO_3Na \rightarrow Ar\cdot + Na_2S_2O_6 \quad (2.2)$$

$$Na_2S_2O_6 \rightarrow Na_2SO_4 + SO_2 \quad (2.3)$$

$$Ar\cdot + Ar\cdot \rightarrow Ar\text{-}Ar \quad (2.4)$$

First, the cleavage of P-tolyl-sulfonate bonds occur, while corresponding aryl (Ar) and sulfite radicals are also generated. The sulfite radicals could substitute for aryl (Ar) radicals to form the stable $Na_2S_2O_6$. Then the disproportionation decomposition reaction of $Na_2S_2O_6$ will finally form the $Na_2SO_4$. To sum, the dual-sulfur doping, namely sulfur-containing functional group and ultrafine sulfates, has been successfully synthesized and characterized.

To assess the electrochemical performance of DS-CN and S-CB, we assemble CR2016 coin cells with potassium foil. Fig. 4**a and b** exhibit the cyclic voltammetry (CV) measurement curves of the two different carbonization products. In the case of DS-CN, the two reversible CV peaks located at 0.75 and 1.75 V can be observed, which are ascribed to reversible capture of $K^+$ at S-containing functional groups sites [44]. In the subsequent CV cycles, an apparent overlap can be observed, which means good cycle stability and reversibility. In contrast to the CV of DS-CN, during the first potassiation of S-CB, an obvious irreversible peak can be observed at about 0.7 V, due to the influence of surface functional groups, the formation of solid electrolyte interphase (SEI) membrane and the irreversible electrochemical trapping of micropores [38]. Moreover, another strong cathodic peak close to 0.01 V is related to the intercalation of $K^+$ into S-CB [48].

Fig. 4**c and d** reveal the first three cycles of DS-CN and S-CB at 100 mA $g^{-1}$. And a significant irreversible capacity appears during the first discharge, due to the similar reasons in above-mentioned CV part. In addition, the DS-CN anode shows a great discharge and charge capacity (529.3 and 271.4 mA h $g^{-1}$) for the initial cycle, which is twice higher than the S-CB anode (263.6 and 93.0 mA h $g^{-1}$). Moreover, the initial Coulombic efficiency (CE) of DS-CN (51.3%) is higher than that of S-CB (35.2%). This phenomenon is related to the oxygen content (4.21 at% for DS-CN, 27.54 at% for S-CB), since excess oxygen functional groups usually cause many irreversible reactions in the first cycle [36].

Fig. 4**e** shows the cycling performance and CE of DS-CN and S-CB at 100 mA $g^{-1}$. For DS-CN, after 200 cycles, the reversible capacity can still maintain 242.8 mA h $g^{-1}$ with a capacity retention of 93.7% (against 10th discharge capacity). However, for S-CB, the reversible capacity is merely 90.6 mA h $g^{-1}$. Obviously, better cycle performance can be revealed for DS-CN electrode, which may be related to the higher S/O ratio and extra capacity from $Na_2SO_4$ [36,49]. In addition, the two different materials demonstrate low CE during the first cycle, which is ascribed to the formation of more SEI layers and irreversible

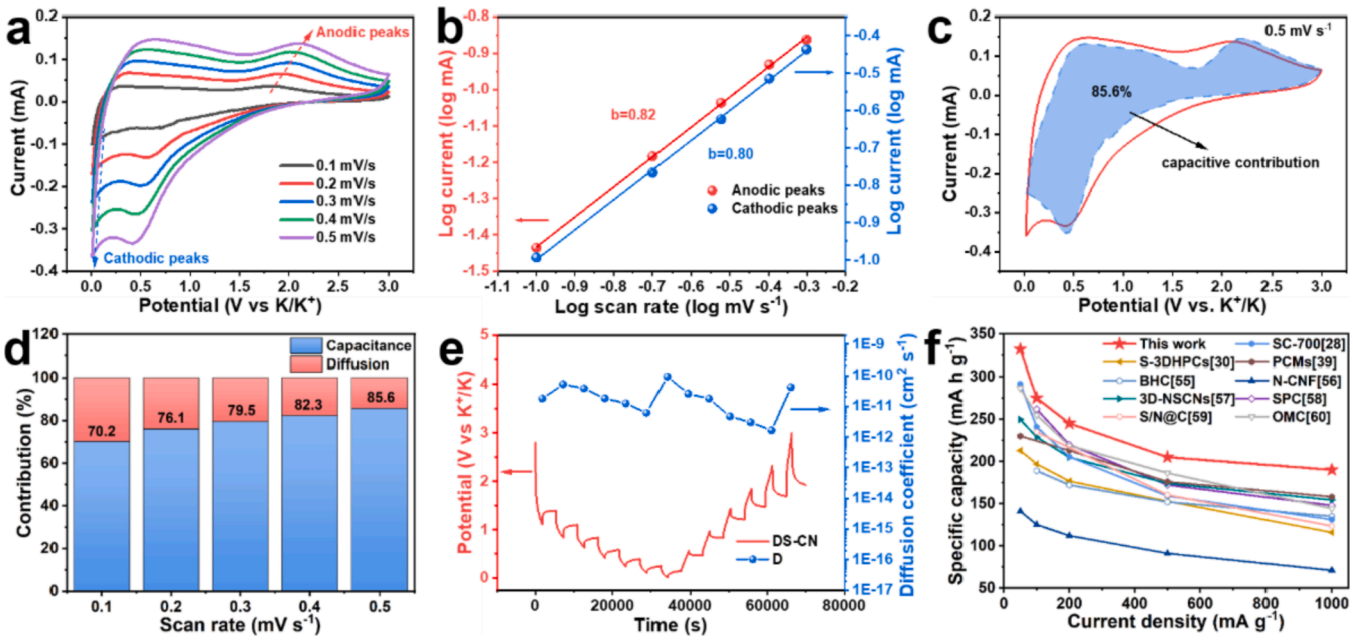


**Fig. 5.** Quantitative analysis to confirm the kinetics of DS-CN: (a) CV curves at different scan rates; (b) Calculated *b*-value for the anodic peaks and cathodic peaks; (c) CV curve and the corresponding capacitive contribution illustrated by the blue region; (d) Normalized contribution ratios of capacitance and diffusion at different scan rates; (e) The GITT curve and the calculated $K^+$ chemical diffusion coefficients; (f) Rate performances and capacities of different carbon-based materials. (For interpretation of the references to colour in this figure legend, the reader is referred to the web version of this article.)

electrochemical adsorption originated from the porous structure with large specific surface area. And this phenomenon is usually observed in the carbon-based materials [50,51]. Remarkably, expect for the first a few cycles, the subsequent CE of DS-CN stabilizes at around 100%, but S-CB exhibits a lower CE during whole cycles.

Significantly, the DS-CN exhibits superior rate capability and long cycling stability. Fig. 4**f**, Fig. S9a and b show the capacity of DS-CN and S-CB electrodes at various current densities. The average reversible capacities of DS-CN are 331.9, 275.0, 244.3, 205.0, 165.3 mA h $g^{-1}$ at 50, 100, 200, 500, 1000 mA $g^{-1}$, respectively. However, the corresponding reversible capacities of S-CB are 154.9, 103.1, 66.0, 24.8, 10.3 mA h $g^{-1}$, respectively. Besides, when the current density of 100 mA $g^{-1}$ is applied again, the DS-CN anode regains a reversible capacity of 277.5 mA h $g^{-1}$ with a high-capacity retention of 100.9%. These results indicate the DS-CN anode possesses the great rate performance and cycling stability. Furthermore, the long-term cyclability of DS-CN electrode was measured at a large current density of 1000 mA $g^{-1}$ (Fig. 4**g** and Fig. S9c). Remarkably, even after 1500 cycles, DS-CN is still able to deliver the capacity of 189.2 mA h $g^{-1}$ and shows a high-capacity retention of 83.2% (based on the capacity of the tenth cycle), indicating 0.011% capacity decrease per cycle. Besides, the CE is close to 100% except first a few cycles, which indicates good stable reversibility. In addition, the electrochemical impedance spectroscopy (EIS) measurements of DS-CN and S-CB anodes are shown in Fig. S10. It indicates a lower charge transfer resistance of DS-CN, which enhances the intercalation/deintercalation of $K^+$ and charge transfer.

To further investigate the kinetics and electrochemical reaction mechanism, CV measurements (Fig. 5**a** and Fig. S11a) were carried out at various scan rates (0.1 – 0.5 mV $s^{-1}$). It is clearly seen that at different scan rates, the shape of the CV curves also maintains. The current ($i$) and scan rate ($v$) can be fitted by the power-law relationship [52]:

$$i(v) = av^b \tag{2.5}$$

$$log(i) = blog(v) + loga \tag{2.6}$$

In the equation, $a$ and $b$ are constants and the $b$ value is related to the reaction kinetics during the process of ion storage. It is a classic diffusion-controlled process (intercalation) if the $b$ value is 0.5. As the $b$ value is 1, it displays a surface capacitive-controlled process, also known as pseudocapacitive behavior [52]. The calculated $b$ values for DS-CN are 0.82 (anodic peaks) and 0.80 (cathodic peaks) respectively (Fig. 5**b**), while they are 0.67 (anodic peaks) and 0.50 (cathodic peaks) for S-CB (Fig. S11b), respectively. The result indicates that it is mainly a surface capacitive-controlled process for DS-CN. To further research the contribution of the different kinetics process to the whole capacity, the corresponding signal feedback at a specific potential ($V$) could be further analyzed by the following relationship [53] :

$$i(V) = k_1 v + k_2 v^{1/2} \tag{2.7}$$

where $k_1$ and $k_2$ are variable parameters. The $k_1 v$ stands for the surface capacitive-controlled process, while $k_2 v^{1/2}$ is corresponding to the diffusion-controlled process. In Fig. 5**c**, the blue region implies the surface capacitive-controlled process of DS-CN anode at the scan rate of 0.5 mV $s^{-1}$. By calculating the area of blue region, the contribution rate of the surface capacitive-controlled process is 85.6%. Fig. 5**d** summarizes the capacitive contributions of DS-CN anode at different scan rates. It can be found that the capacitive contribution increases from 70.2% to 85.6% following the scan rate increases from 0.1 mV $s^{-1}$ to 0.5 mV $s^{-1}$, which is much higher than those of S-CB anode (Fig S11c). The results further confirm the ion-storage process of DS-CN is mainly controlled by the pseudocapacitive behavior. The surface capacitive-controlled features of DS-CN contribute to enhance $K^+$ adsorption and vibrant kinetics.

To further investigate the $K^+$ diffusivity ($D_K{}^+$), the galvanostatic intermittent titration technique (GITT) was conducted (Fig. 5**e** and Fig. S11d) [44,54]. And the $D_K{}^+$ can be calculated for DS-CN and S-CB anodes during the potassiation process from 3.0 to 0.01 V. For DS-CN, the values of $D_K{}^+$ are $1.67 \times 10^{-12} - 9.30 \times 10^{-11}$. And it is worth noting that the $D_K{}^+$ are slightly larger than those of S-CB, indicating that the transport of $K^+$ of DS-CN is facilitated. Furthermore, to better demonstrate the rate performance and capacity, the comparison with other carbon-based anode materials for KIBs is presented in Fig. 5**f**. Clearly, DS-CN exhibits the excellent rate performance and capacity among them [28,30,39,55–60].

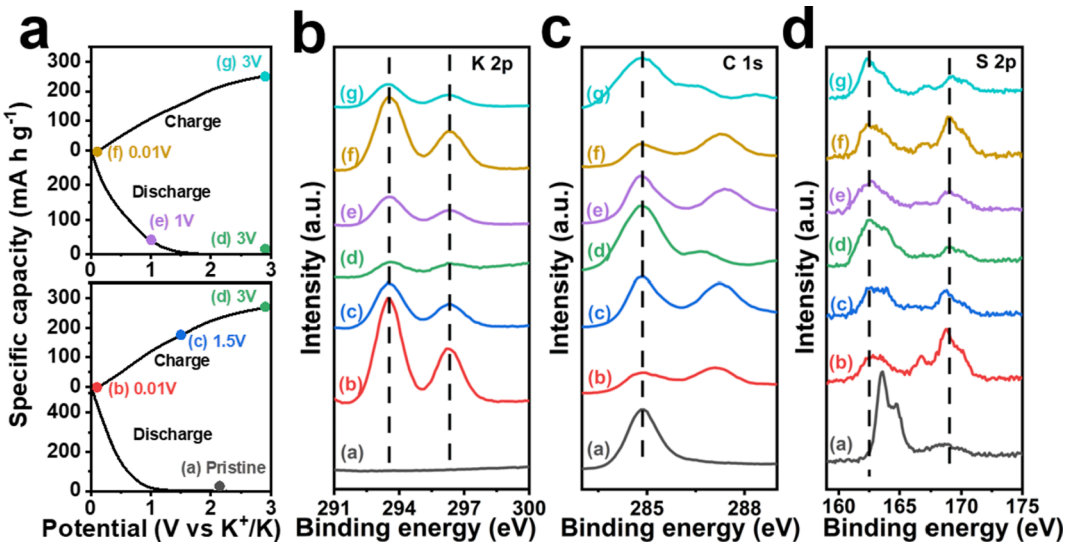


**Fig. 6.** *Ex-situ* XPS of DS-CN in different intercalation/deintercalation states during first two charge–discharge cycles: (a) the corresponding voltage position; (b) K 2p, (c) C 1s, (d) S 2p XPS spectra.

To get in-depth understanding of the (de)potassiation mechanism of DS-CN, *ex-situ* XPS analysis (Fig. 6**a**) was carried out at different stages during the initial two cycles. From K 2p spectra (Fig. 6**b**), during first discharge, two peaks at about 293.3 and 296.0 eV are present, indicating the presence of K-C bonds induced by the intercalation of $K^+$ into DS-CN [61]. After the first potassiation process, the two peaks can still be observed due to some irreversible reactions, for example, the electrolyte decomposes then reacts with $K^+$ to form SEI film [38]. During the second cycle, the K 2p peaks change periodically, indicating the potassiation reactions with carbon are reversible.

The XPS C 1s spectra are shown in Fig. 6**c**, and for peaks located at 284.8, 285.1, 286.0 and 289.6 eV, and the four peaks stand for C–C, C-K, C-S and O-C=O bonds respectively (Fig. S12) [35,44]. Obviously, the intensities of C-K and C-S bonds are the highest when discharge to 0.01 V, while those are the lowest when charge to 3 V, which indicate a repeated evolution. It is noted that after the second depotassiation, the XPS peaks have similar shapes with those after the first depotassiation, indicating the stable reversibility.

In addition, Fig. 6**d** presents the XPS S 2p spectra, revealing the change of S during the (de)potassiation process. In the discharge of the first cycle, it can be observed that the intensity of thiophene-type S (C-S) decreases while that of oxidized-type S (-C-$SO_2$-) increases, which demonstrates that doped S reacts with potassium reversibly [38]. It is striking to note that during the (de)potassiation process, the peak of thiophene-type S negatively shifts to a lower value, since the strong interactions between $K^+$ and S atoms result in the transition of S to a lower state [44,62]. It has been shown in previous studies that S site works as "bridge" to facilitate the reaction between C-S bonds and $K^+$ to form C-S-K bonds, which can provide more potassium storage sites and higher potassium storage capacity [38].

## 3. Conclusion

In summary, we use a cheap and mass-produced chemical product ($CH_3C_6H_4SO_3Na$) as the precursor to obtain DS-CN by a simple one-step carbonization method. Compared with S-CB, the DS-CN provides a larger layer spacing to adapt the intercalation/deintercalation of $K^+$, and has a higher S/O ratio to reduce the irreversible capacity caused by oxygen functional groups. Benefiting from that, DS-CN exhibits a high reversible capacity (242.8 mA h $g^{-1}$ at 100 mA $g^{-1}$), long cycle stability (0.011% capacity decay per cycle during 1500 cycles) and good rate performance. More importantly, the increase of its capacity can be attributed to the reaction between C-S bonds and $K^+$ to form C-S-K bonds. Furthermore, the ultrafine $Na_2SO_4$ in DS-CN can provide more -C-$SO_2$- bond so as to provide more adsorption capacity. This work can provide a new feasible and effective way strategy to develop low-cost, high-performance carbon-based anode materials for KIBs and other electrochemical energy storage applications.

## Declaration of Competing Interest

The authors declare that they have no known competing financial interests or personal relationships that could have appeared to influence the work reported in this paper.

## Acknowledgements

Zijian Li and Xinfei Wu contributed equally to this work. This work was supported by the National Natural Science Foundation of China (51832004, 51904216), National Key Research and Development Program of China (2020YFA0715000), and the National Students Innovation and Entrepreneurship Training Program (WUT: 202010497007).

## Appendix A. Supplementary data

Supplementary data to this article can be found online at https://doi.org/10.1016/j.cej.2021.134207.

## References

[1] H. Li, Z. Wang, L. Chen, X. Huang, Adv. Mater. 21 (2009) 4593–4607.
[2] G. Li, Y. Wang, H. Guo, Z. Liu, P. Chen, X. Zheng, J. Sun, H. Chen, J. Zheng, X. Li, J. Mater. Chem. A 8 (2020) 16920–16925.
[3] K. Kubota, M. Dahbi, T. Hosaka, S. Kumakura, S. Komaba, Chem Rec 18 (2018) 459–479.
[4] Y.L. Wenchao Zhang, Z. Guo, Sci. Adv. 5 (2019) eaav7412.
[5] J.-Y. Hwang, S.-T. Myung, Y.-K. Sun, Adv. Funct. Mater. 28 (2018) 1802938.
[6] K. Fu, J. Chen, R. Xiao, J. Zheng, W. Tian, X. Li, Energy Environ. Sci. 11 (2018) 1563–1570.
[7] H. Huang, R. Xu, Y. Feng, S. Zeng, Y. Jiang, H. Wang, W. Luo, Y. Yu, Adv Mater 32 (2020), e1904320.
[8] X. Zou, P. Xiong, J. Zhao, J. Hu, Z. Liu, Y. Xu, Phys Chem Chem Phys 19 (2017) 26495–26506.
[9] S. Komaba, T. Hasegawa, M. Dahbi, K. Kubota, Electrochem. Commun. 60 (2015) 172–175.
[10] M. Zhou, P. Bai, X. Ji, J. Yang, C. Wang, Y. Xu, Adv Mater 33 (2021), e2003741.
[11] X. Wu, Y. Chen, Z. Xing, C.W.K. Lam, S.S. Pang, W. Zhang, Z. Ju, Adv. Energy Mater. 9 (2019) 1900343.

[12] W. Zhang, Z. Xie, M. Zheng, H. Hu, Y. Xiao, Y. Liu, Y. Liang, Energy Storage Mater. 29 (2020) 300–309.
[13] S. Wang, P. Xiong, X. Guo, J. Zhang, X. Gao, F. Zhang, X. Tang, P.H.L. Notten, G. Wang, Adv. Funct. Mater. 30 (2020) 2001588.
[14] Y. Liang, C. Luo, F. Wang, S. Hou, S.C. Liou, T. Qing, Q. Li, J. Zheng, C. Cui, C. Wang, Adv. Energy Mater. 9 (2018) 1802986.
[15] L. Fan, R. Ma, Q. Zhang, X. Jia, B. Lu, Angew Chem Int Ed Engl 58 (2019) 10500–10505.
[16] L. Liu, Z. Lin, J.-Y. Chane-Ching, H. Shao, P.-L. Taberna, P. Simon, Energy Storage Mater. 19 (2019) 306–313.
[17] Z. Jian, Z. Xing, C. Bommier, Z. Li, X. Ji, Adv. Energy Mater. 6 (2016) 1501874.
[18] W. Miao, X. Zhao, R. Wang, Y. Liu, L. Li, Z. Zhang, W. Zhang, J Colloid Interface Sci 556 (2019) 432–440.
[19] Y. Wang, Z. Wang, Y. Chen, H. Zhang, M. Yousaf, H. Wu, M. Zou, A. Cao, R.P. S. Han, Adv Mater 30 (2018), e1802074.
[20] J. Lin R. Chenna Krishna Reddy, C. Zeng, X. Lin, A. Zeb, C.-Y. Su, Coordination Chemistry Reviews 446 2021 214118.
[21] S. Gong, Q. Wang, The Journal of Physical Chemistry C 121 (2017) 24418–24424.
[22] C. Liu, N. Xiao, H. Li, Q. Dong, Y. Wang, H. Li, S. Wang, X. Zhang, J. Qiu, Chem. Eng. J. 382 (2020), 121759.
[23] B. Huang, S. Liu, X. Zhao, Y. Li, J. Yang, Q. Chen, S. Xiao, W. Zhang, H.-E. Wang, G. Cao, Sci. China Mater. 64 (2020) 85–95.
[24] X. Zhao, F. Gong, Y. Zhao, B. Huang, D. Qian, H.-E. Wang, W. Zhang, Z. Yang, Chem. Eng. J. 392 (2020).
[25] B. Wang, F. Yuan, W. Li, Q. Wang, X. Ma, L. Gu, H. Sun, K. Xi, D. Zhang, W. Wang, NANO Energy 75 (2020), 104979.
[26] W. Xiao, X. Li, B. Cao, G. Huang, C. Xie, J. Qin, H. Yang, J. Wang, X. Sun, NANO Energy 83 (2021).
[27] W. Xiao, Q. Sun, M.N. Banis, B. Wang, W. Li, M. Li, A. Lushington, R. Li, X. Li, T. K. Sham, X. Sun, Adv. Funct. Mater. 30 (2020).
[28] M. Wang, Y. Zhu, Y. Zhang, J. Duan, K. Wang, R. Wang, G. Sun, C. Wang, J. Power Sources 481 (2021), 228902.
[29] J. Yang, Z. Ju, Y. Jiang, Z. Xing, B. Xi, J. Feng, S. Xiong, Adv Mater 30 (2018) 1700104.
[30] S.-X. Yan, Q. Wang, S.-H. Luo, Y.-H. Zhang, X. Liu, Y.-G. Liu, Z.-Y. Wang, A.-M. Hao, T.-F. Yi, J. Power Sources 461 (2020), 228151.
[31] Q. Yu, J. Hu, Y. Gao, J. Gao, G. Suo, P. Zuo, W. Wang, G. Yin, J. Alloy. Compd. 766 (2018) 1086–1091.
[32] Y. Liu, Z. Tai, J. Zhang, W.K. Pang, Q. Zhang, H. Feng, K. Konstantinov, Z. Guo, H. K. Liu, Nat Commun 9 (2018) 3645.
[33] Z. Jian, S. Hwang, Z. Li, A.S. Hernandez, X. Wang, Z. Xing, D. Su, X. Ji, Adv. Funct. Mater. 27 (2017) 1700324.
[34] C. Lu, Z. Sun, L. Yu, X. Lian, Y. Yi, J. Li, Z. Liu, S. Dou, J. Sun, Adv. Energy Mater. 10 (2020).
[35] S. Tian, D. Guan, J. Lu, Y. Zhang, T. Liu, X. Zhao, C. Yang, J. Nan, J. Power Sources 448 (2020), 227572.
[36] J. Ding, H. Zhang, H. Zhou, J. Feng, X. Zheng, C. Zhong, E. Paek, W. Hu, D. Mitlin, Adv Mater 31 (2019), e1900429.
[37] B. Wang, F. Yuan, Q. Yu, W. Li, H. Sun, L. Zhang, D. Zhang, Q. Wang, F. Lai, W. Wang, Energy Storage Mater. 38 (2021) 329–337.
[38] J. Li, W. Qin, J. Xie, H. Lei, Y. Zhu, W. Huang, X. Xu, Z. Zhao, W. Mai, NANO Energy 53 (2018) 415–424.
[39] M. Chen, W. Wang, X. Liang, S. Gong, J. Liu, Q. Wang, S. Guo, H. Yang, Adv. Energy Mater. 8 (2018) 1800171.
[40] B. Qu, W. Hu, L. Deng, W. Sun, S. Ding, Z. Gan, S. Su, Energy Fuels 30 (2016) 8561–8566.
[41] G. Lente, I. Fabian, Inorg. Chem. 43 (2004) 4019–4025.
[42] T. Meissner, F. Eisenbeiss, B. Jastorff, J. Chromatogr. A 838 (1999) 81–83.
[43] Y. Qian, S. Jiang, Y. Li, Z. Yi, J. Zhou, J. Tian, N. Lin, Y. Qian, Energy Storage Mater. 29 (2020) 341–349.
[44] L. Tao, Y. Yang, H. Wang, Y. Zheng, H. Hao, W. Song, J. Shi, M. Huang, D. Mitlin, Energy Storage Mater. 27 (2020) 212–225.
[45] S.Y. Li, H.L. Deng, Z.L. Chu, T. Wang, L. Wang, Q.S. Zhang, J.H. Cao, Y.L. Cheng, Y. Q. Huang, J. Zhu, B.A. Lu, ACS Appl Mater Interfaces 13 (2021) 50005–50016.
[46] Y. Peng, Z. Chen, R. Zhang, W. Zhou, P. Gao, J. Wu, H. Liu, J. Liu, A. Hu, X. Chen, Nanomicro Lett 13 (2021) 192.
[47] A.D. Roberts, X. Li, H. Zhang, Carbon 95 (2015) 268–278.
[48] C. Lv, W. Xu, H. Liu, L. Zhang, S. Chen, X. Yang, X. Xu, D. Yang, Small 15 (2019), e1900816.
[49] D. Li, X. Ren, Q. Ai, Q. Sun, L. Zhu, Y. Liu, Z. Liang, R. Peng, P. Si, J. Lou, J. Feng, L. Ci, Adv. Energy Mater. 8 (2018) 1802386.
[50] X. Wu, Y. Chen, Z. Xing, C.W.K. Lam, S.S. Pang, W. Zhang, Z. Ju, Adv. Energy Mater. 9 (2019).
[51] Y. Wu, H. Zhao, Z. Wu, L. Yue, J. Liang, Q. Liu, Y. Luo, S. Gao, S. Lu, G. Chen, X. Shi, B. Zhong, X. Guo, X. Sun, Energy Storage Mater. 34 (2021) 483–507.
[52] V. Augustyn, J. Come, M.A. Lowe, J.W. Kim, P.L. Taberna, S.H. Tolbert, H. D. Abruna, P. Simon, B. Dunn, Nat Mater 12 (2013) 518–522.
[53] D. Luo, J. Xu, Q. Guo, L. Fang, X. Zhu, Q. Xia, H. Xia, Adv. Funct. Mater. 28 (2018) 1805371.
[54] K. Tang, X. Yu, J. Sun, H. Li, X. Huang, Electrochimica Acta 56 (2011) 4869–4875.
[55] W. Yu, Z. Liu, X. Yu, B. Lu, Adv. Energy and Sustainability Research 2 (2021) 2100018.
[56] L. Ma, J. Li, Z. Li, Y. Ji, W. Mai, H. Wang, Nanomaterials (Basel) 11 (2021) 1130.
[57] Y. Zhang, S. Tian, C. Yang, J. Nan, Dalton Trans 49 (2020) 5108–5120.
[58] L. Wang, S. Li, J. Li, S. Yan, X. Zhang, D. Wei, Z. Xing, Q. Zhuang, Z. Ju, Mater. Today Energy 13 (2019) 195–204.
[59] A. Mahmood, S. Li, Z. Ali, H. Tabassum, B. Zhu, Z. Liang, W. Meng, W. Aftab, W. Guo, H. Zhang, M. Yousaf, S. Gao, R. Zou, Y. Zhao, Adv Mater 31 (2019), e1805430.
[60] W. Wang, J. Zhou, Z. Wang, L. Zhao, P. Li, Y. Yang, C. Yang, H. Huang, S. Guo, Adv. Energy Mater. 8 (2018) 1701648.
[61] X.-R. Li, F.-Y. Kong, J. Liu, T.-M. Liang, J.-J. Xu, H.-Y. Chen, Adv. Funct. Mater. 22 (2012) 1981–1988.
[62] R. Ma, L. Fan, J. Wang, B. Lu, Electrochimica Acta 293 (2019) 191–198.